

This is the **accepted version** of the journal article:

Ros, Carles; Murcia López, Sebastián; Garcia, Xènia; [et al.]. «Facing seawater splitting challenges by regeneration with Ni–Mo–Fe bifunctional electrocatalyst for hydrogen and oxygen evolution». ChemSusChem, Vol. 14, issue 14 (July 2021), p. 2872-2881. DOI 10.1002/cssc.202100194

This version is available at <https://ddd.uab.cat/record/271928>

under the terms of the  ^{IN} COPYRIGHT license

Facing seawater splitting challenges by regeneration with Ni-Mo-Fe OER/HER bifunctional electrocatalyst

Dr. Carles Ros,^{a,*} Dr. Sebastian Murcia-López,^a Xenia Garcia,^b Marcos Rosado,^c Prof. Jordi Arbiol,^{c,d} Prof. Jordi Llorca,^b, Prof. Joan R. Morante^{a,e}

^a Catalonia Institute for Energy Research (IREC). Jardins de les Dones de Negre 1, 08930 Sant Adrià del Besòs, Barcelona, Spain

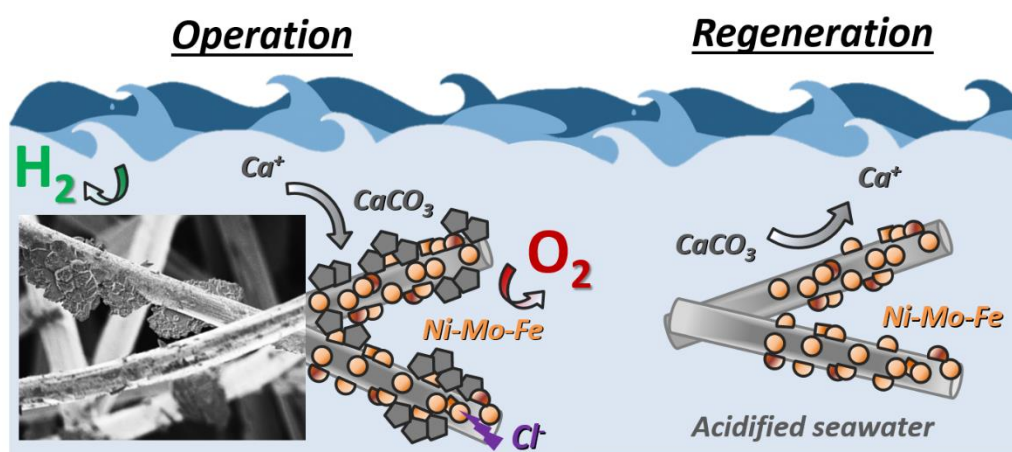
^b Institute of Energy Technologies, Department of Chemical Engineering and Barcelona Research Center in Multiscale Science and Engineering, Universitat Politècnica de Catalunya, EEBE, Eduard Maristany 10-14, 08019 Barcelona, Spain

^c Catalan Institute of Nanoscience and Nanotechnology (ICN2), CSIC and BIST, Campus UAB, Bellaterra, 08193 Barcelona, Catalonia, Spain

^d ICREA, Pg. Lluís Companys 23, 08010 Barcelona, Catalonia, Spain

^e Universitat de Barcelona (UB), Martí i Franquès, 1, 08028 Barcelona, Spain

TOC AND TOC TEXT



Hydrogen from seawater: a highly efficient Ni-Mo-Fe electrocatalyst deposited on non-expensive carbon felts is reported stable in seawater as electrolyte. Cl⁻ pitting is suppressed in alkalized electrolyte and CaCO₃ precipitation on the electrodes is reverted by a simple regeneration technique. Stability over 24 h, 300 mA·cm⁻² productivities and water splitting

voltage down to 1.59 V are shown. This approach makes seawater splitting promising and economically feasible.

KEYWORDS

NiMoFe, seawater, water splitting, regeneration, degradation, hydrogen

ABSTRACT

Hydrogen, produced by water splitting, has been proposed as one of the main green energy vectors of the future if produced from renewable energy sources. However, to substitute fossil fuels, large amounts of pure water are necessary, scarce in many world regions. In this work, we fabricate efficient and earth-abundant electrodes, study the challenges of using real seawater and propose an electrode regeneration method to face undesired salts deposition.

Ni-Mo-Fe trimetallic electrocatalyst is deposited on non-expensive graphitic carbon felts both for HER and OER in seawater and alkaline seawater. Cl^- pitting and the chlorine oxidation reaction are suppressed on these substrates and alkalized electrolyte. Precipitations on the electrodes, mainly CaCO_3 , originated from seawater dissolved components have been studied and a simple regeneration technique is proposed to rapidly dissolve undesired deposited CaCO_3 in acidified seawater. Under alkaline conditions, Ni-Mo-Fe based catalyst is found to reconfigure, under cathodic bias, into Ni-Mo-Fe alloy with a cubic crystalline structure and Ni:Fe(OH)_2 redeposits whereas, under anodic bias, it is transformed into a follicular Ni:FeOOH structure. High productivities over $300 \text{ mA}\cdot\text{cm}^{-2}$ and voltages down to 1.59 V @ $10 \text{ mA}\cdot\text{cm}^{-2}$ for the overall water splitting reaction have been shown, and electrodes are found stable for over 24 h without decay in alkaline seawater conditions and with energy efficiency higher than 61.5% which makes seawater splitting promising and economically feasible.

INTRODUCTION

Hydrogen generated from water splitting is a promising candidate to substitute fossil fuels as green energy vector. For global scale hydrogen production, a large water source is needed, and simultaneously the world is expected to face significant clean water scarcity in several territories[1]. Most works have studied acidic or alkaline deionized water, but such purification process introduces costs to large scale usage[2] together with requiring large scale desalinization plants with huge investment and considerable operation costs. Seawater, instead, represents 96.5% of Earth's water, but contains several dissolved salts (about 0.5 M Na^+ and Cl^- , in lower but significant quantities SO_4^{2-} , Mg^+ and Ca^+ , and several other elements traces[3]) and organic components, with a pH close to neutral, ranging between 7.5 and 8.4[4]. Seawater splitting would offer the possibility of distributed implementation of electrolyzers close to any water source with reduced water treatment costs.

The main challenges seawater electrolysis faces are the highly corrosive Cl^- pitting of several metals, competing chlorine oxidation and dissolved anions and cations deposition at the surface, deactivating the catalysts[3,5] and also blocking light, what would diminish productivity if photoelectrodes are used[6–9].

Chlorine corrosion of metals[10] like steel or nickel[11–13], named 'pitting', is widely known in industry, mainly due to the need to protect metallic boats, marine platforms and bridges from corrosion in seawater. It is based on an autocatalytic process where defects (pits) on the metal are present. This process forms a local acidic pH in these pits that enhances metallic cation migration and sustains the dissolution. Many parameters affect the thermodynamics and kinetics of this dissolution process: pH and the presence of other ions such as sulfates and bromine have significant effects on the reaction[14]; applied potentials and specific alloying

such as steel with molybdenum[15], for example, and alkaline (oxidative) electrolytes forming passive superficial films can inactivate this electrochemical corrosion reaction[16,17].

For electrolysis in neutral pH, even at low applied currents, ion migration is difficult to compensate and local pH significantly varies up to ± 4 pH points, especially for insufficiently buffered solutions in the 4-10 pH range[18,19]. This has a significant role also when a secondary competing reaction is possible, like chlorine oxidation - evolution reaction (CIER), happening between 130 and 480 mV more anodic than oxygen evolution reaction (OER) for pH 0 and 14, respectively[20]. This is known as the 'alkaline design criterion' in saline water electrolysis. More specifically, local pH in front of anodes can reach significantly acidic pH values, reducing the thermodynamic overpotential for CIER and enhancing hypochlorous acid formation, a corrosive agent[20]. In front of cathodes, local pH variation can cause the deposition or precipitation of $\text{Ca}(\text{OH})_2$ and $\text{Mg}(\text{OH})_2$. [21]

This behavior is different under alkaline conditions. At high pH, in a Cl^- containing electrolyte, local pH modifications are expected to be significantly faster compensated by the high OH^- concentration[19], what also enhances the HER and OER reactions[22,23]. Moreover, in these conditions, CIER presents the highest overpotential with respect to OER (~ 480 mV)[20]. Increasing the pH also causes part of the ions dissolved in seawater (Ca^+ , Mg^+) to precipitate as hydroxides[21], reducing their detrimental effects.

Hypochlorite (which partially reacts and evaporates as Cl_2 gas) and chlorine gas formation itself, apart from corrosion problems, are sub products of a side reaction to hydrogen production in saline water. However, there is not enough industrial demand for chlorine to be considered as an alternative to OER in systems aiming at substitution of fossil fuels by hydrogen, and it cannot be massively released to the atmosphere as it is a toxic gas[24]. Thus, its production must be avoided. For it, reactor designs, electrode substrates and electrocatalysts

must be fabricated with corrosion-resistant materials and are required to perform with overpotentials lower than CIER[25]. Also, earth abundant and cost-effective materials are required for worldwide electrolysis deployment[26,27].

Until now, only few works have studied seawater splitting. Among them, some have studied the challenges of neutral pH electrolysis with fabricated bifunctional HER/OER electrodes performing $<1.9\text{ V @ }10\text{ mA}\cdot\text{cm}^2$ in pH 7 neutral buffered electrolytes[28] which means energy efficiency conversion of higher than 60% but at low production rate. Moreover, the nickel foam-based electrodes used, fail after few hours when exposed to (chlorine-containing) seawater[28,29].

Some works have been capable to protect nickel-based electrodes with overlayers for alkalized and Cl^- -containing water or seawater splitting, obtaining significant productivities. Kuang *et al.*[30] were capable to protect a nickel foam anode from Cl^- corrosion with a nickel–iron hydroxide (NiFe) electrocatalyst layer uniformly coated on a nickel sulfide (NiS_x) layer, which was capable of sustaining up to $1\text{ A}\cdot\text{cm}^2$ in $1\text{ M KOH} + 0.5\text{ M NaCl}$ with an overall water splitting voltage of 2.45 V. It achieves high hydrogen productivity although the conversion energy efficiency decreases to 50%. Alternatively, Yu *et al.*[31] covered nickel foam with NiMoN nanorods with a NiFeN shell and stabilized it for $1\text{ M KOH} + 0.5\text{ M NaCl}$ and $1\text{ M KOH} + \text{seawater}$ electrolytes. They point in the detection of some deactivation in the anode due to the deposition of some insoluble precipitates from alkalized seawater. Although electrodes have also been fabricated on Ti substrates[32,33], resistive TiO_2 formation in the interlayer could not be entirely prevented for long term experiments in 0.5 M NaCl [34].

Very few works have used carbon substrates with Cl^- or seawater based electrolytes, although it is a highly stable and non-expensive material used in harsh environments and highly developed for flow cell batteries[35,36]. For example, Gupta *et al.*[37] studied OER

electrolysis with bimetallic oxy-boride (Co-Fe-O-B) on glassy carbon in 1 M KOH + 0.5 M NaCl, although a 45% current loss is observed after 20h.

In the present work, Ni-Mo-Fe based electrocatalysts have been deposited on graphitic carbon felts. Both carbon and selected catalytic metals (Ni, Mo and Fe) are cheap and relatively earth abundant materials[38], which together with the felt-like porous and high surface area substrate configuration, are ideal for large scale implementation in static or flow cell configurations. In alkaline electrolytes, Ni-Fe[39,40] and Ni-Mo[41,42] based catalysts are known to be among the best-performing earth abundant ones for OER and HER, respectively[43]. A trimetallic alloy of Ni-Mo-Fe has been previously studied as efficient bifunctional electrocatalyst in alkaline media[44] and, hence, it could open the possibility of significantly cheaper hydrogen production by seawater splitting if the difficulties for working with sea water can be overcome. To analyze these challenges, electrodes were tested in different electrochemical conditions: i) filtered real seawater, ii) alkalized real seawater (adding 0.5 M KOH), iii) simulated alkaline seawater (0.5 M NaCl + 0.5 M KOH) and iv) alkaline pure water (0.5 M KOH) as basic reference. These electrolytes have been selected to compare the effects of seawater dissolved salts and the advantages of alkalizing it. Moreover, herein used graphitic carbon felt substrates fulfill the requirements concerning conductivity, stability and electrochemical and geometrical areas ratio, widely used for flow cell configurations[45–47].

We have put special attention to the behavior of the Ni-Mo-Fe proposed electrocatalysts used as anodes and cathodes in the previously described different electrolyte conditions. A structural reorganization of the trimetallic catalyst and dissolved ion related precipitation/deposition is studied. Neutral filtered seawater is shown to produce significant Cl⁻ etching of Ni, Fe and Mo, in anodic conditions and abundant CaCO₃ precipitate in cathodic polarization. Meanwhile seawater alkalization enables higher productivities and long lasting stability. Furthermore, stability has also been enhanced applying a regeneration technique that facilitate the

elimination of calcium carbonate deposition on the electrodes based on an acid treatment step that allows cleaning the electrodes. These results will for sure help in increasing the knowledge of seawater impurities effect on electrocatalysis and developing electrocatalytic devices to work in real seawater for long term water splitting with minimal water purification costs (under 0.0072€ per kg of H₂) enabling a cheap hydrogen production route without concerns on consuming the scarce fresh water for human use.

MATERIALS AND METHODS

Ni-Mo-Fe electrodes were prepared by simultaneous electrodeposition on deionized (D.I.) water rinsed 3 x 1 cm² graphitic carbon felt electrodes (SIGRACELL® GFD 2,5 EA from SGL Carbon industries) with only 1 x 1 cm² immersed in the precursor solution. The electrodeposition process was adapted from Ni-Mo electrodeposition[42], where the precursor solution was prepared by adding 0.15 M Fe(SO₄) · 7 H₂O to 0.3 M NiSO₄ · 6 H₂O + 0.2 M Na₂MoO₄ · 2 H₂O + 0.3 M Na₃C₆H₅O₇ · 2 H₂O, pH adjusted to 10.5 with NH₄OH. The electrodeposition was performed at -100 mA·cm⁻² for 20 min. Samples are later rinsed in D.I. water and dried in N₂ flow. Ni foam electrodes used as comparative reference for the graphitic carbon felt substrates were cut to 1x3 cm² pieces from Ni-4753 produced by Recemat and simply rinsed in D.I. water prior to use.

Special graphite counter electrodes and holders (1940 Electrographite, Mersen) are used to avoid any metallic part being in contact with the electrolytes or generated vapors. Sample and holder device are depicted in Fig. S.1.

SEM images were obtained with a Zeiss Series Auriga Field Effect Scanning Electron Microscope (FESEM) and XHRSEM Magellan 400L equipped with EDX. Structural characterization was carried out by X-ray diffraction (XRD) in a D8 Advance Bruker

equipment with a Cu K α radiation source working at 40 kV and 40 mA. ATR spectra was obtained with a Bruker Alpha-P FT-IR spectrometer. Surface chemical characterization was done by X-ray Photoelectron Spectroscopy (XPS) on a SPECS system equipped with a XR50 source operating at 300 W and a Phoibos 150 MCD-9 detector. Al K α X-ray source has been employed for XPS measurements. The pass energy of the hemispherical analyzer was set at 20 eV and the energy step of high-resolution spectra was set at 0.1 eV. Binding energy (BE) values were referred to the C 1s peak at 284.8 eV. Data processing was performed with the CasaXPS software. Atomic fractions were calculated using peak areas normalized on the basis of acquisition parameters after background subtraction, experimental sensitivity factors and transmission factors provided by the manufacturer.

Three-electrode electrochemical measurements were obtained with a Biologic VMP-300 potentiostat using Ag/AgCl/KCl(3M) ($E^0 = 0.205 \text{ V}_{\text{RHE}}$) as reference electrode and graphite electrode as counter electrode. i) Filtered seawater (SW), ii) alkalized seawater (A-SW, adding 0.5 M KOH to filtered seawater), iii) alkaline saline pure water (AS-PW, 0.5 M NaCl + 0.5 M KOH) and iv) alkaline pure water (A-PW, 0.5 M KOH) were used as electrolytes. The seawater was obtained from the seaside of Barcelona the 11th of June, 2020, and was filtered with 200 nm nylon filters to remove any particles, microbial organisms, etc. Acidified seawater was prepared by adding 0.5 M H₂SO₄ to filtered seawater (SW). Alkalized seawater (A-SW) was prepared by adding 0.5 M of KOH to the filtered seawater, where significant precipitate is generated, and was centrifuged at 11.000 rpm for 5 min to separate the solid precipitate, and further filtered with 200 nm nylon filters. The seawater (SW), alkalized seawater (A-SW) and solid precipitate are analyzed in the supporting information. Ion chromatography was performed using a Dionex IonPack AS22 diluting 100x in D.I. water the analyzed electrolyte samples. Electrochemical impedance spectroscopy was obtained with 10 mV amplitude and scanning from 1 MHz to 1 Hz.

Seawater alkalization: purification and its precipitates

Precipitate obtained after introducing KOH pellets (0.5 M) to real seawater (Fig. S.2) was dried and measured by XRD (Fig. S.3) and FTIR-ATR (Fig. S.4), where it is quantified by XRD to be about a 31% of $\text{Ca}(\text{OH})_2$ and a 69% of $\text{Mg}(\text{OH})_2$, being Ca^{2+} and Mg^{2+} two of the main ions in seawater[3]. FTIR-ATR also confirmed the hydroxides presence by the OH^- stretching at 3700 cm^{-1} peak, and characteristic peaks at ~ 1439 and $\sim 827\text{ cm}^{-1}$ for $\text{Ca}(\text{OH})_2$ [48] and ~ 1381 and $\sim 1650\text{ cm}^{-1}$ for $\text{Mg}(\text{OH})_2$ [49]. Thus, the alkalization process causes a reduction in the Ca and Mg ion content in seawater, what should be expected to reduce precipitate deposition at electrode's surface. pH measurements show a pH variation from roughly measured $\text{pH}_{\text{AS-PW}} = \sim 13.7$ to $\text{pH}_{\text{A-SW}} = \sim 13.6$, thus the hydroxide concentration reduction is calculated to be $\Delta[\text{OH}^-] \approx -0,1\text{ M}$ lower than AS-PW. Thus, for continuous operation, if 1 L of seawater is replenished after 1 L of H_2O is converted into H_2 and O_2 , extra 0.1 mol of OH^- must be added to sustain the herein presented method. We roughly calculated a cost introduced by alkalizing seawater, corresponding to the precipitated portion, of 0.0072€ per kg of H_2 produced, using NaOH (equivalent and cheaper than KOH) bought at an industrial price of 0.31€/kg[50].

RESULTS AND DISCUSSION

Graphitic carbon felts were selected as substrates after proving stable in 0.5 M NaCl, 0.5 M KOH and 0.5 M NaCl + 0.5 M KOH, while Ni foam suffered from chlorine pitting (Fig. S.5, S.6 and S.7). Ni-Mo-Fe catalysts were deposited on graphitic carbon felts by an electrodeposition method. The trimetallic alloy electrochemical behavior is compared to Ni-Mo[41,42] and Ni-Fe[39,40] in 0.5 M KOH electrolyte (Fig. S.8), some of the best-reported

HER and OER catalysts, respectively, in alkaline electrolysis[51]. Ni-Mo-Fe presents an excellent compromise as it performs as good as Ni-Fe in OER and almost as Ni-Mo in HER.

The trimetallic Ni-Mo-Fe alloy was measured in A-PW, AS-PW, A-SW and SW electrolytes by cyclic voltammetries and for 20 h at a fixed $50 \text{ mA}\cdot\text{cm}^{-2}$ current (Fig. 1a and b) and at a fixed voltage (Fig. S.9). All samples present significant stability over 24 h except the anodes measured in SW.

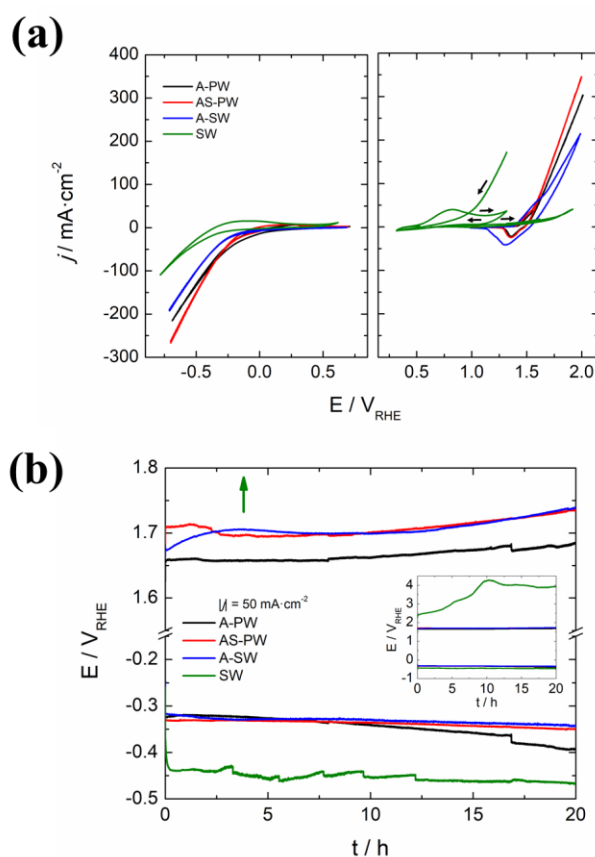


Fig. 1: a) cyclic voltammograms from -0.7 to 0.6 V vs RHE (cathodes) and from 0.3 to 2 V vs RHE (anodes) and b) chronopotentiometries at $50 \text{ mA}\cdot\text{cm}^{-2}$ fixed current for Ni-Mo-Fe decorated graphitic carbon felt electrodes. pH of the SW electrolyte varied from 7.9 to about 11.5 and the RHE potential was corrected based on the latter.

In seawater (SW, pH 7.9), significant decay of the oxidative reaction (anode) is observed in the 0.5 – 1.2 V vs RHE range (lower than OER potential), which corresponds to Cl^- pitting of the trimetallic alloy[13], dissolving the catalysts (Fig. 1a). Electrodes are polarized up to 2 V vs RHE, but performance stays significantly low due to the catalyst pitting suffered. Moreover, at these higher potentials CIER is expected to be favorable evolving Cl^- into Cl_2 gas and hypochlorite, modifying the pH and further enhancing the corrosion of the trimetallic alloy[10]. When set at a fixed current, the anodic overpotential increases drastically (Fig 1b, inset), with observable significant carbon dissolution due to such high potentials applied in the anode to maintain the $50 \text{ mA}\cdot\text{cm}^{-2}$. Moreover, when set at a fixed voltage (Fig. S.9) for 24 h in SW, the anodic current decreases to zero within the first hours, due to etching of the metal catalyst, and the OER overpotential increases significantly in the remaining “bare” substrate (up to 4 V vs RHE, Fig. 1b). On the other hand, the HER reaction has a higher overpotential (expected for a near-neutral pH HER reaction) but is stable in this measurement range. Significant change in the pH of the electrolyte is measured after 24 h stability measurements (from $\text{pH}_i \sim 7.9$ to $\text{pH}_f \sim 11.5$), caused by hypochlorite formation, and precipitate is observed.

Meanwhile, when tested in alkaline electrolytes (A-PW, AS-PW and A-SW), there is no fast deactivation observed, and cyclic voltammograms present characteristic $\text{Ni}^{2+/3+}$ redox peaks, partially overlapping with OER as side-effect of Fe impurities presence[39]. For $100 \text{ mA}\cdot\text{cm}^{-2}$ currents, about 400-500 mV overpotentials are obtained. Alkaline electrolytes are known to form passivation layers against chlorine corrosion by forming oxidized surfaces in the form of hydroxides or oxy-hydroxides[16,17]. In these conditions, voltages down to 1.59 V @ $10 \text{ mA}\cdot\text{cm}^{-2}$ for all alkaline electrolytes and 2 V @ $100 \text{ mA}\cdot\text{cm}^{-2}$ for A-PW and AS-PW and 2.19 V @ $100 \text{ mA}\cdot\text{cm}^{-2}$ for A-SW for the overall water splitting reaction are obtained (Fig. 1a), with electrochemical efficiencies of 77, 61 and 55 %, respectively. Tafel slopes have been measured, being 229.4, 256.1, 234.2 and 201.6 mV/dec for A-PW, AS-PW, A-SW and SW electrolytes

respectively at cathodic potentials, and 41.8, 36.0 and 95.4 mV/dec for A-PW, AS-PW and A-SW electrolytes respectively at anodic potentials. Series resistance has been quantified by EIS, accounting for ionic transport resistance and electrode's electrical resistance, and results have been iR corrected to prove that overpotentials, in the electrochemical surface, do not reach the CIER starting overpotential of +480 mV in alkaline electrolytes and thus, no chlorine gas or hypochlorite production are expected (Fig. S.10). This was also measured by ion chromatography, and no CIER products were detected after 24 h of Ni-Mo-Fe vs Ni-Mo-Fe at $100 \text{ mA}\cdot\text{cm}^{-2}$ in AS-PW (Fig. S.11). In this case, only a slight increase of the Cl^- peak, attributed to a decrease of total water content caused by the sustained water splitting during 24 h, resulting in an increase of the Cl^- concentration, proving again Cl^- is not consumed.

As can be observed, the behavior is similar but slightly varies depending on the used electrolytes. The slight higher currents obtained in AS-PW with respect to A-PW can be attributed to higher conductivity of the electrolyte due to the higher ionic concentration. Seawater + 0.5 M KOH (A-SW) presents lower currents.

The lower performance with A-SW as electrolyte can be attributed to the presence of significant impurities in seawater, a high ionic strength of the ions present in seawater and the precipitation of material during alkalization, resulting in less OH^- present. As described by Bigiani *et al.*[52], impurities present in seawater can block the electrocatalyst surface and also higher ionic strength of seawater compared with the artificial one can decrease the availability of H_2O or OH^- required for OER in the electrode/electrolyte interface[53]. Moreover, the precipitation of dissolved ions in the form of hydroxides when KOH is added to sea water (Fig. S.2) results in lower alkalinity of the electrolyte. The amount of precipitated hydroxides is calculated in Materials section *Seawater alkalization: purification and its precipitates*.

Ni-Mo-Fe electrocatalyst deposition and reconfiguration under different electrolyte and polarization conditions.

SEM (Fig. 2a and Fig. S.12) image of the after-electrodeposited samples reveal two different structures electrodeposited, a porous thin film (Fig. S.12c and gray in Fig. 2a) covering the major part of the carbon fibers (dark gray in Fig. 2a) and some agglomerates on top of it (clear gray in Fig. 2a). EDX mapping (Fig. 2b to f) shows both the porous thin film and the agglomerated structures apparently homogeneously composed of Ni-Mo-Fe-O, with Ni being the most abundant metal after deposition, Fe has a lower concentration and Mo is the lowest, according to EDX signal intensity.

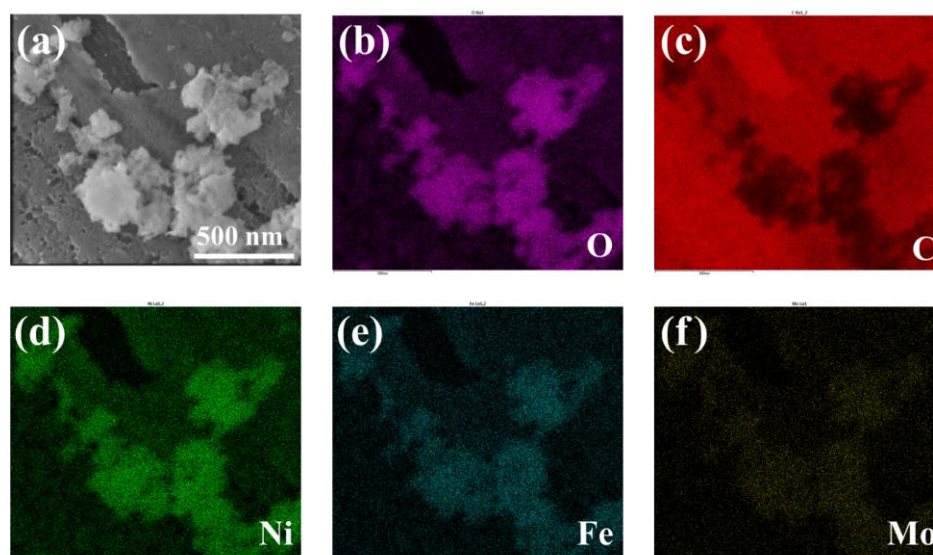


Fig. 2: a) SEM image of an as-deposited Ni-Mo-Fe catalyst on a graphitic carbon felt. a-fi) EDX maps of the region in a).

After set in working conditions for 24 h in the various electrolytes, significant changes are observed (Fig. 3 and S.13 to S.20). In A-PW and AS-PW (Fig 3a-d), samples polarized at anodic potentials (1.7 V vs RHE) electrolytes present follicular structures, resembling known oxy-hydroxide structures for Ni-Fe-OOH[54]. This significant dissolution/re-electrodeposition

and redistribution observed has been previously also reported for nickel iron hydroxides[40,55,56].

Instead, the electrodes polarized at cathodic potentials (-0.4 V vs RHE) in these two electrolytes present reconfiguration into a nanoparticles-covered surface. Two kinds of nanoparticles are observed, with different apparent density (brighter by SEM Fig. 3a and c, a sign of being denser). The EDX colored composed map of Fig. 4 and Fig. S.17 clearly shows the two kinds of particles present. The cubic particles are identified as consisting of Mo and Fe, with low amount of Ni and O, and the non-cubic ones, less dense, to contain Ni with higher amount of O, traces of Fe and no Mo. This points in the direction of having segregation into Ni-Mo-Fe alloy in a cubic crystalline structure[41] and Ni(OH)₂ redeposition, known to form these kind of bumps[54] (with traces of Fe).

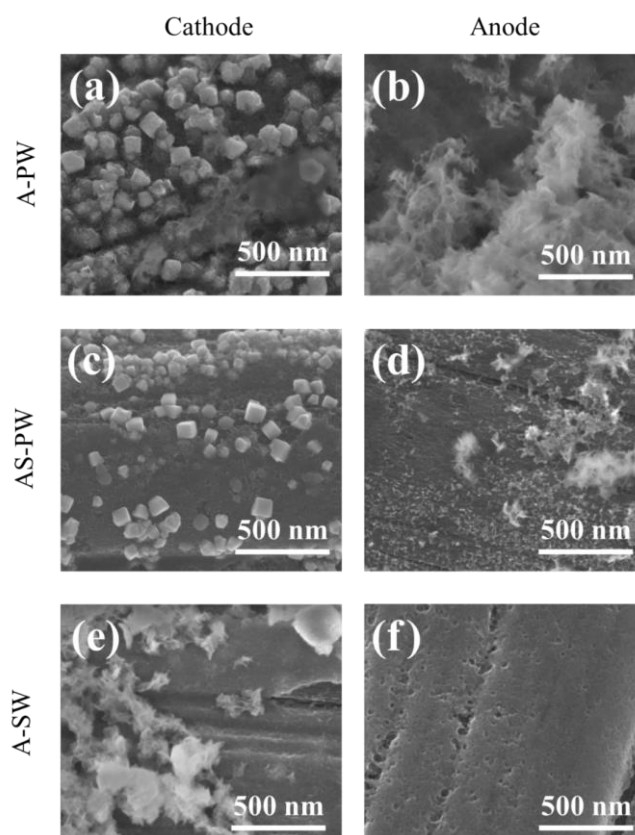


Fig. 3: SEM images with 200kX magnification of Ni-Mo-Fe decorated electrodes cycled in different electrolytes and cathodic and anodic polarizations.

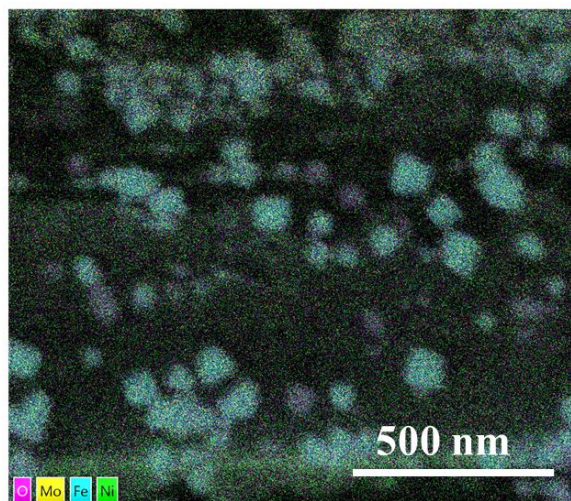


Fig. 4: SEM-EDX map of the Fig. 3c, cycled in AS-PW and polarized as a cathode for 20 h, presenting two different-composition particles according to EDX spectra: ones consisting of Mo and Fe, with low amount of Ni and O, and the others containing Ni with higher amount of O, traces of Fe and no Mo. The non-overlapped elemental map can be observed in Fig. S.17.

Ni-Mo-Fe was also deposited on transparent substrates (fluorine doped tin oxide, FTO), where a significant change in the transparency of the samples was observed (Fig. S.21 and S.22). Electrodes measured as cathodes present lower transparency than the ones measured as anodes. This also points in the direction of the trimetallic alloy being present in an oxidized state when working as anode and a more reduced one, less transparent (more metallic), when working as cathode.

XPS measurements of the binding energy range corresponding to the catalyst elements, together with oxygen and carbon, from as-deposited samples and after 20 h in operation in A-PW, AS-PW and A-SW electrolytes conditions are presented in Table S.1 and S.2. Initially, the catalyst metallic fraction is measured to be composed at its surface by a 57% of Ni, 31% Mo and 12% Fe (Table S.2). The elemental composition of samples after working conditions is similar for all of the studied alkaline electrolytes, in average 77% Ni, 3% Mo and 20% Fe,

and thus, we can observe a significant Mo loss. There is a slight tendency of Mo being more present in samples which have been measured in cathodic conditions for all 3 electrolytes, which is in accordance with the data from EDX maps (Fig S.15 to S.20). Regarding the Ni/Fe ratio, we observe a slight decrease of Ni (from 4.75 to 3.85) after 20 h of operation, which could be attributed both to imprecision of measurement or slight dissolution[57] into the electrolyte up to equilibrium.

From XPS analysis, an increase of the carbon (C 1s) signal together with an increased sp^2 carbon (C-C characteristic of graphitic carbon) signal[58,59] detected can be observed for samples used for 20 h in electrolytes compared with as-deposited samples (Table S.1 and representative electrodes are shown in Fig. S.23 and S.24). This is attributed to the loss or restructuring of the metallic films, leaving an increased graphitic (sp^2 C-C) carbon felts surface exposed for A-PW and AS-PW electrolytes, but not for A-SW, where a film of deposited salt is observed as previously mentioned. O 1s peak (Table S.3) shows higher amount of hydroxides after using the electrodes, an effect of the alkaline electrolyte on metals, and lower metal-oxide bonds in the case of samples used as anodes, an additional sign of restructuring and metal-hydroxide formation. Ni 2p_{3/2} lineshapes and binding energy positions (Table S.4) suggest a predominance of Ni(OH)₂ phase contributions over NiFe₂O₄ and NiO for samples #3 and #5, whereas the contribution of the NiFe₂O₄ phase could increase in the other samples and thus balance the contributions of the different Ni phases, according to the literature[60,61]. In all cases, the spin-energy separation between Ni2p_{3/2} and Ni2p_{1/2} peaks is ≈ 17.4 eV, which indicates the presence of Ni²⁺ oxidation state."Mo 3d_{5/2} and 3d_{3/2} signal, show Mo⁶⁺ to be a 38% in as-deposited samples and reduced significantly in used samples, leaving a major percentage of Mo⁵⁺ in used samples although an overall Mo loss (Table S.5). Mo has been reported to slowly dissolve in anodic alkaline conditions[62], it is believed that the high electrode potential during OER can oxidize low-valence Mo species to

soluble Mo^{6+} compounds[44]. The Fe 2p signal is too close to the baseline noise signal, and a proper fit cannot be obtained. Beyond this, all used samples appear highly oxidized in the outmost superficial layers analyzed by XPS, due to being immersed in highly alkaline electrolytes and the observed differences between the different polarizations are not showing any major trends. There is no clear trend caused by Cl^- presence in the electrolyte affecting the trimetallic alloys composition, only small Mo fraction reduction confirmed both by XPS and EDX. Although, there is a lower Fe composition for both polarizations in A-SW conditions.

XRD diffractograms of the as-deposited samples are shown in Fig. S.25, where substrate's graphitic peaks are observed (26.2 , 43.9 and 54.6° , JCPDS #00-003-0401) together with a peak at 35.7° which can be indexed to a nickel-iron oxide with significantly low crystallinity (JCPDS #00-010-0325). One must note as-deposited materials by room-temperature electrodeposition are usually highly amorphous and is difficult to observe clear XRD peaks. After measuring for hours in different electrolytes, Ni-Mo-Fe trimetallic electrodes (Fig. 5) present the graphitic substrate's wide peaks, traces of both NiOOH structure (11.43°) and a peak at $\sim 43.5^\circ$ which is an overlapping of the second peak of graphite and signal from a cubic crystalline structure of metallic Ni[41]. Even if there was no overlapping with graphite, there would be small difference between alloys of Fe or Mo with Ni (JCPDS #03-065-5480 for MoNi_4 and # 38-0419 for FeNi_3)[63,64] as the dominating peaks correspond to cubic structure of metallic Ni. The peak at 11.43° corresponding to $\text{Ni}(\text{OH})_2/\text{NiOOH}$ (JCPDS #01-089-7111) is not present in as-deposited samples (Fig. S.26) and clearly appearing in all samples immersed in alkaline electrolytes (Fig. 5), but not on neutral-pH seawater, which is in accordance of this phase forming in high-pH electrolytes.

As mentioned, Mo content is detected by EDX and XPS analysis to significantly decrease, more accentuated after alkaline OER conditions. Part of Mo is also reported by other works to dissolve in the electrolyte, meanwhile remaining Ni, Fe and Mo reconfigure into NiFeMo

(oxy)hydroxide after oxygen evolution process[44]. Detected Mo loss in anodic alkaline conditions is not expected to significantly affect electrode performance in OER, as Ni-Fe is already known to be excellent OER catalyst in alkaline conditions[43] given by Fe introducing a partial-charge-transfer activation effect on Ni, even when only Fe traces are present[39]. Meanwhile, for alkaline HER conditions, the remaining Mo present in the Ni-Mo-Fe alloy (clearly visible by EDX), forms the previously mentioned cubic crystalline nanoparticles, simultaneous to Ni(OH)₂ redeposited bumps. Efficient HER catalysis in alkaline conditions given by Ni-Mo-based catalysts[43] is reported to be caused by an increased hydrogen adsorption[65], a synergistic effect[41] of Mo oxo species acting as active sites on a Ni conductive and anchoring structure, also preventing Mo dissolution and modifying the electronic structure of the Mo surface species[66].

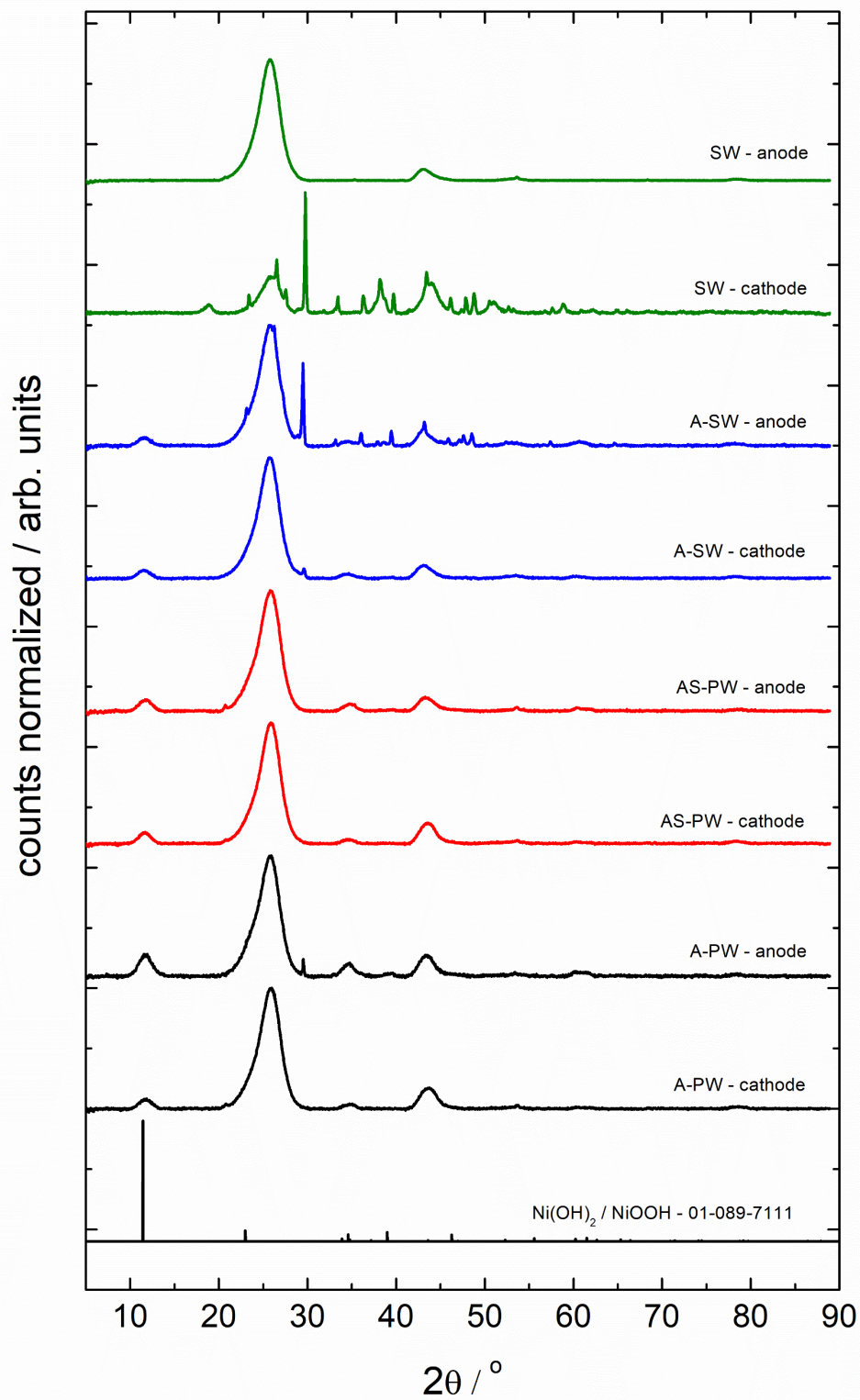


Fig. 5: XRD diffractogram of Ni-Mo-Fe decorated graphitic carbon felt electrodes after 20 h in different electrolytes and polarizations, together with the JCPDS peaks of Ni(OH)₂/NiOOH.

The effects of seawater dissolved ions: CaCO₃ deposition

In A-SW, characterized by the presence of other ions, mainly Ca²⁺, significant differences are observed compared with A-PW and AS-PW. As can be seen in Fig. 3e, some follicular structures are observed in cathodic conditions, together with some dense nanoparticles. A thin overlayer has been deposited, originating from dissolved ions in seawater, over the electrocatalyst nanoparticles. In Fig. S.27 this overlayer is partially detached, exposing the graphitic carbon felt and the electrocatalyst nanoparticles below. Ni and Fe are detected, in all of these structures, with traces of Mo (Fig. S.19). Differently, in anodic conditions, a thin film covering all surface is observed with A-SW (Fig. 3f). Correlating these results with XRD (Fig 5 and Fig. 7), we are detecting CaCO₃ deposited during operation conditions.

In the case where SW is used as electrolyte, the changes observed are very clear. In the cathodic side a large amount of precipitate accumulates (Fig. 6a and b), covering the fibers and presenting granular grown structures and a thin film covering all the fibers surface. Looking at spots where the film was detached, some bright particles could be seen beneath resembling original Ni-Mo-Fe catalyst. Cathodes are capable to work for 24 h with only about a 20% decrease in performance (Fig. 1b and Fig. S.9), meaning this large amount of precipitate does not completely block catalyst activity. In the anodic side (Fig. 6c, d), no precipitate is observed, neither any trace of the catalyst Ni-Mo-Fe films; by the color of the electrolyte, strong metallic dissolution (Cl⁻ pitting) is happening, as will be further discussed.

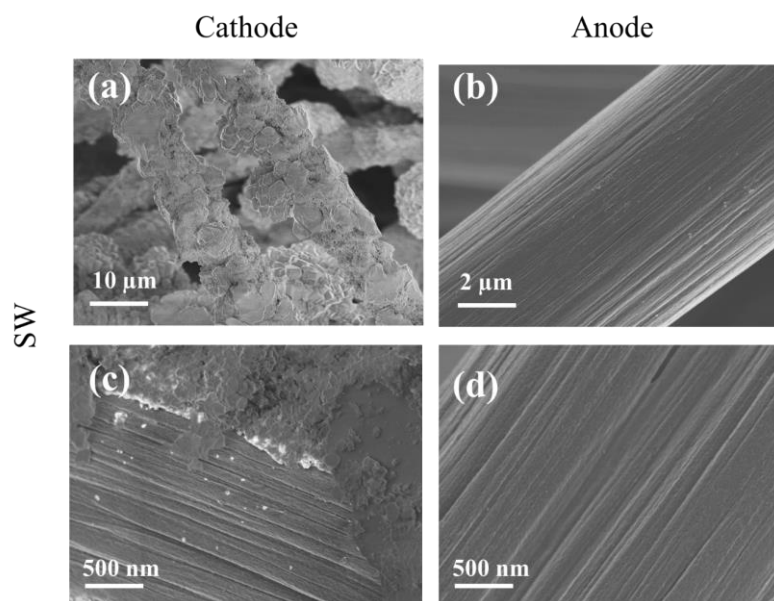


Fig. 6: SEM images of a and b) a cathode and c and d) an anode after 20 h in working conditions using SW as electrolyte.

The material deposited is analyzed by XRD, significantly more intense in SW cathodes (Fig. 5 and 7). Similar deposition is observed on NiMoFe using FTO as substrates (Fig. S.26). A specific analysis depicted in Fig. 7 shows the contamination when using the electrode in SW is composed of calcium carbonate (CaCO_3) both in the calcite rhombohedral and orthorhombic aragonite crystalline orientations, and magnesium hydroxide ($\text{Mg}(\text{OH})_2$) brucite. Meanwhile, when working with A-SW, only the rhombohedral calcite CaCO_3 is detected with a smaller signal. This can be explained due to a lower ions concentration after alkalization and a major precipitation of $\text{Mg}(\text{OH})_2$ when adding the 0.5 M KOH (Fig. S.2 and S.3), having this Mg ion and the pH a key role in the crystalline orthorhombic aragonite structure formation for CaCO_3 [67].

The precipitation either at the anode or cathode can be explained, in the case of SW, due to the local pH increase in front of the cathode, promoting hydroxide formation and precipitation of the dissolved ions, while in front of the anode a more acidic pH is created, which would promote the CaCO_3 dissolution into Ca^{2+} and CO_2 . Also, a more acidic local pH for anodes in

neutral-pH seawater also shifts the CIER reaction to lower overpotentials[20], and thus, form hypochlorites which, simultaneously to the presence of Cl^- , can dissolve metallic catalysts such as Ni-Mo-Fe. This explains the “cleaned” graphitic carbon felt surface observed in Fig. 6c and d. In the case of A-SW precipitate is observed in both anode and cathode (Fig. 3e and f) although forming different structures. Regarding XRD (Fig. 5), in the anode CaCO_3 appears to form a more crystalline structure meanwhile less crystallinity is detected in the cathode.

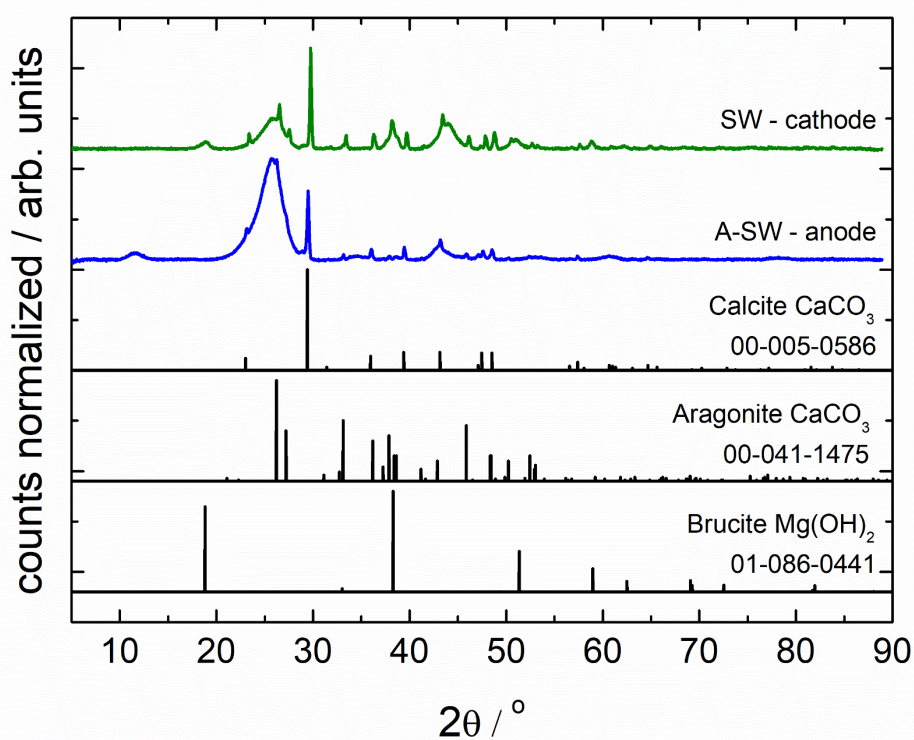


Fig. 7: XRD diffractogram of Ni-Mo-Fe decorated graphitic carbon felt electrodes after 20 h in SW polarizing as cathode and in A-SW polarizing as an anode, compared to the JCPDS of calcite and aragonite CaCO_3 and brucite $\text{Mg}(\text{OH})_2$.

Ni-Mo-Fe electrodes were measured in different temperature conditions in A-SW, and as expected, the total water splitting voltage for both HER and OER half-reactions necessary to

work at $100 \text{ mA}\cdot\text{cm}^{-2}$ decreased from 2.16 V at 30 °C to 1.86 V at 70 °C, a 32% overvoltage reduction (Fig. S.28) increasing the energy efficiency from 56% to 66%. The role of temperature should be further studied in future work, as it is key in reducing electrochemical overvoltage[68] and also in the solubility of CaCO_3 [68], thus can play also a role in electrodes deactivation or reactivation.

Electrode regeneration: CaCO_3 dissolution in acid

A regeneration method based on dissolution of CaCO_3 in acid (acidified seawater by adding 0.5 M H_2SO_4 to filtered seawater) was studied, based in immersing the electrodes (after 20 h in operation conditions) for 20 min in the acid. By submerging the electrode with the precipitate on the surface in the acidified seawater, CaCO_3 is observed to instantaneously dissolve by the reaction $\text{CaCO}_3 + \text{H}_2\text{SO}_4 \rightarrow \text{CaSO}_4 + \text{CO}_2 + \text{H}_2\text{O}$, clearly visible by the CO_2 bubbling. Electrodes were tested after the cleaning procedure (Fig. 8) and were found not to be affected when acting as cathodes (both for SW and A-SW) but they are when used as anodes (in A-SW). While for cathodes the CaCO_3 is removed by the acid without harming the HER performance, in the anodic case, the difference is substantial: we observe a shift of the OER reaction to higher overpotentials. Also, the $\text{Ni}^{2+/3+}$ redox peaks, which previously were significantly larger and overlapped with the OER reaction, after immersing in acid appear smaller and more separated from the OER. This change clearly points in the direction of Fe, which was previously coordinated with Ni, being etched during the process[39]. Fe is known to increase and shift the $\text{Ni}^{2+/3+}$ peaks up to overlapping with the OER curve, and also to be a key ion enabling efficient OER catalysis even down to impurity-level concentrations[40,56]. The etch of Fe due to the acidic regeneration technique, thus, causes higher OER overpotentials and reduces $\text{Ni}^{2+/3+}$ peaks and separates them from OER current.

Thus, the regeneration was possible for cathodes after working in SW and A-SW, probably because Fe (etched by the acid) does not play a role in cathodic HER conditions, while, in the anodes case, an overvoltage of 100 mV is introduced. H_2SO_4 regeneration is expected to introduce minimal costs to overall seawater splitting due to the cheap price of this acid (~59 \$/MT[69]) and the low amount used (no pH change was observed after electrode regeneration in 0.5 M H_2SO_4), and cheaper acids could be used. Further work should be performed regarding regeneration methods to find a chemical dissolution of CaCO_3 not dissolving the Fe or alternative OER electrocatalysts not based on Fe, like $\text{Co}_3\text{O}_4/\text{MnO}_2$ [25]. Performing seawater splitting in hotter water, as commented in previous section and shown in Fig. S.28, would increase hydrogen productivity and also help in reducing the detrimental CaCO_3 deposition, as its solubility increases significantly[68]. Short-period hot water flows could also be used to regenerate the electrodes. The costs associated to increase seawater temperature are difficult to speculate and highly dependent to reactor design, thus out of the scope of this work.

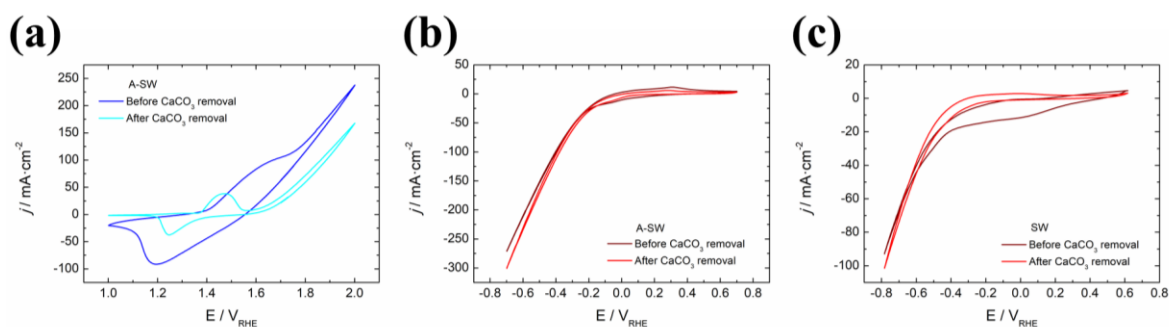


Fig. 8: cyclic voltammeteries of Ni-Mo-Fe decorated electrodes before and after applying the seawater + 0.5 M H_2SO_4 CaCO_3 removal procedure to a) an anode and b) a cathode in A-SW and c) a cathode in SW.

CONCLUSIONS

Ni-Mo-Fe trimetallic alloys deposited on graphitic carbon felt substrates, cheap and earth abundant materials, have been demonstrated as efficient bifunctional catalysts for seawater splitting, presenting catalytic performances as good as Ni-Fe in OER and almost as Ni-Mo in HER. A simple one step electrodeposition process was used. Voltages down to 1.59 V @10 mA·cm⁻² and 2.16 V @100 mA·cm⁻² at room temperature and 1.86 V @100 mA·cm⁻² at 70 °C for the overall water splitting reaction are obtained with alkalized seawater, achieving an energy efficiency of 77, 55 and 66% respectively, stable for over 24 h without significant degradation.

Under alkalized conditions, EDX and XPS analyses show reorganization of the deposited material into two different morphologies under HER conditions: Ni-Mo-Fe cubic crystalline structure and Ni(OH)₂ bump-like structures (with traces of Fe), known to form from Ni redeposition. In OER conditions, a more follicular structure is found, characteristic of Ni:FeOOH, the more active catalyst specie in alkaline anodic conditions. Electrodes are stable and highly productive both for HER and OER in high pH (~13.5) seawater.

Using neutral seawater as electrolyte (pH ~7) presents significant challenges both by the large amount of carbonate deposition on cathodes and harsh corrosion conditions for anodes caused by Cl⁻ and low competing ClER overpotential. Thus, alkalization of the seawater was found mandatory to avoid corrosion of the deposited metallic catalysts by the formation of a passivation hydroxide superficial layer. Also, the alkalization process enhances the OER over ClER, thus inhibiting Cl₂ gas or hypochlorite formation. Moreover, the alkalization process was found to be a facile and low cost technique to significantly reduce the salinity of the electrolyte, precipitating significant portions of Mg²⁺ and Ca²⁺.

Even so, CaCO_3 was found to deposit on electrodes surface. Although it appears porous and electrodes are not deactivated in the tens of hours' scale, large amounts accumulated during long term operation can reduce performance and block the porosity of graphitic carbon felts.

A regeneration technique to dissolve the CaCO_3 was applied, consisting in immersion of the electrodes in acidified seawater. Immediate dissolution of CaCO_3 was proven, and electrodes performance was not affected when acting as cathodes but an overvoltage of 100 mV is introduced in the anodes case. Analyzing the cyclic voltammetries, a clear sign of Fe loss is observed due to the acidic treatment. Therefore, the acidic technique should be adapted to regenerate anodes or alternative materials to Fe should be studied.

ASSOCIATED CONTENT

Supporting Information. Device photos, cyclic voltammetries, analysis of the precipitate after adding 0.5 M KOH to seawater, XRD, FTIR-ATR, SEM, and EDX supporting images are supplied in an additional document.

AUTHOR INFORMATION

Corresponding Author

*Corresponding authors:

E-mail: cros@irec.cat

Tel: (34) 933 562 615

Author Contributions

The manuscript was written through contributions of all authors. All authors have given approval to the final version of the manuscript.

Funding Sources

ACKNOWLEDGMENT

Authors from IREC acknowledge Generalitat de Catalunya for financial support through the CERCA Programme. J.R.M. acknowledge Generalitat de Catalunya for financial support through the CERCA Programme, M2E (2017 SGR 1246). IREC and ICN2 also acknowledge additional support by the European Regional Development Funds (ERDF, FEDER) and by MINECO coordinated project ENE2017-85087-C3. ICN2 was supported by the Severo Ochoa program from Spanish MINECO (Grant No. SEV-2017-0706) and is funded by the CERCA Programme/Generalitat de Catalunya. ICN2 acknowledge funding from Generalitat de Catalunya SEV-2017-0706). JL and XG are grateful to projects MICINN/FEDER RTI2018-093996-B-C31 and Generalitat de Catalunya 2017 SGR 128. XG is grateful to Generalitat de Catalunya for PhD grant 2017 FI_B 00137. JL is a Serra Húnter fellow and is grateful to ICREA Academia program.

REFERENCES

- [1] P. Gracia-de-Rentería, G. Philippidis, H. Ferrer-Pérez, A.I. Sanjuán, Living at the water's edge: A world-wide econometric panel estimation of arable water footprint drivers, *Water (Switzerland)*. 12 (2020). <https://doi.org/10.3390/W12041060>.
- [2] G. Matute, J.M. Yusta, L.C. Correas, Techno-economic modelling of water electrolyzers in the range of several MW to provide grid services while generating

- hydrogen for different applications: A case study in Spain applied to mobility with FCEVs, *Int. J. Hydrogen Energy*. 44 (2019) 17431–17442.
<https://doi.org/10.1016/j.ijhydene.2019.05.092>.
- [3] S. Dresp, F. Dionigi, M. Klingenhof, P. Strasser, Direct electrolytic splitting of seawater: Opportunities and challenges, *ACS Energy Lett.* 4 (2019) 933–942.
<https://doi.org/10.1021/acseenergylett.9b00220>.
- [4] R. Chester, T. Jickells, *Marine geochemistry*, 2012. <https://doi.org/10.1007/3-540-32144-6>.
- [5] W. Tong, M. Forster, F. Dionigi, S. Dresp, R. Sadeghi Erami, P. Strasser, A.J. Cowan, P. Farràs, Electrolysis of low-grade and saline surface water, *Nat. Energy*. (2020).
<https://doi.org/10.1038/s41560-020-0550-8>.
- [6] C. Ros, N.M. Carretero, J. David, J. Arbiol, T. Andreu, J.R. Morante, Insight into the Degradation Mechanisms of Atomic Layer Deposited TiO₂ as Photoanode Protective Layer, *ACS Appl. Mater. Interfaces*. 11 (2019) 29725–29735.
<https://doi.org/10.1021/acsaami.9b05724>.
- [7] C. Ros, T. Andreu, S. Giraldo, V. Izquierdo-Roca, E. Saucedo, J.R. Morante, Turning earth abundant kesterite-based solar cells into efficient protected water splitting photocathodes, *ACS Appl. Mater. Interfaces*. 10 (2018) 13425–13433.
<https://doi.org/10.1021/acsaami.8b00062>.
- [8] C. Ros, T. Andreu, M.D. Hernández-Alonso, G. Penelas-Pérez, J. Arbiol, J.R. Morante, Charge Transfer Characterization of ALD-Grown TiO₂ Protective Layers in Silicon Photocathodes, *ACS Appl. Mater. Interfaces*. 9 (2017) 17932–17941.
<https://doi.org/10.1021/acsaami.7b02996>.

- [9] C. Ros, T. Andreu, S. Giraldo, Y. Sánchez, J.R. Morante, Conformal chalcopyrite based photocathode for solar refinery applications, *Sol. Energy Mater. Sol. Cells.* 158 (2016) 184–188. <https://doi.org/10.1016/j.solmat.2016.01.031>.
- [10] United States Department of the Interior, Saline water conversion report, 1970.
- [11] S. Hinnov, J. Tamm, The effect of halide ions on nickel corrosion in perchloric acid solutions, *Proc. Est. Acad. Sci.* 60 (2011) 184–192. <https://doi.org/10.3176/proc.2011.3.07>.
- [12] J.R. de Alda¹, S. Ahn², D.D. Macdonald³, H. Kwon², The Role of Chloride Ion in Passivity Breakdown on Nickel and Chromium, (n.d.) 62515.
- [13] M. Abdallah, B.A. AL Jahdaly, M.M. Salem, A. Fawzy, A.A. Abdel Fattah, Pitting corrosion of nickel alloys and stainless steel in chloride solutions and its inhibition using some inorganic compounds, *J. Mater. Environ. Sci.* 8 (2017) 2599–2607.
- [14] M.B. Ives, Y.C. Lu, J.L. Luo, Cathodic reactions involved in metallic corrosion in chlorinated saline environments, *Corros. Sci.* 32 (1991) 91–102. [https://doi.org/10.1016/0010-938X\(91\)90065-W](https://doi.org/10.1016/0010-938X(91)90065-W).
- [15] H.J. Grabke, M. Spiegel, A. Zahs, Role of alloying elements and carbides in the chlorine-induced corrosion of steels and alloys, *Mater. Res.* 7 (2004) 89–95. <https://doi.org/10.1590/s1516-14392004000100013>.
- [16] F. Arjmand, A. Adriaens, Influence of pH and chloride concentration on the corrosion behavior of unalloyed copper in NaCl solution: A comparative study between the micro and macro scales, *Materials (Basel).* 5 (2012) 2439–2464. <https://doi.org/10.3390/ma5122439>.
- [17] H. DorMohammadi, Q. Pang, P. Murkute, L. Árnadóttir, O.B. Isgor, Investigation of

- chloride-induced depassivation of iron in alkaline media by reactive force field molecular dynamics, *Npj Mater. Degrad.* 3 (2019). <https://doi.org/10.1038/s41529-019-0081-6>.
- [18] M. Auinger, I. Katsounaros, J.C. Meier, S.O. Klemm, P.U. Biedermann, A.A. Topalov, M. Rohwerder, K.J.J. Mayrhofer, Near-surface ion distribution and buffer effects during electrochemical reactions, *Phys. Chem. Chem. Phys.* 13 (2011) 16384–16394. <https://doi.org/10.1039/c1cp21717h>.
- [19] I. Katsounaros, J.C. Meier, S.O. Klemm, A.A. Topalov, P.U. Biedermann, M. Auinger, K.J.J. Mayrhofer, The effective surface pH during reactions at the solid-liquid interface, *Electrochem. Commun.* 13 (2011) 634–637. <https://doi.org/10.1016/j.elecom.2011.03.032>.
- [20] F. Dionigi, T. Reier, Z. Pawolek, M. Gliach, P. Strasser, Design Criteria, Operating Conditions, and Nickel-Iron Hydroxide Catalyst Materials for Selective Seawater Electrolysis, *ChemSusChem*. 9 (2016) 962–972. <https://doi.org/10.1002/cssc.201501581>.
- [21] B. Bulletin, The Precipitation of Calcium and Magnesium from Sea Water by Sodium Hydroxide Author (s): Eleanor M . Kapp Reviewed work (s): Published by : Marine Biological Laboratory, 55 (2013) 453–458.
- [22] L. Giordano, B. Han, M. Risch, W.T. Hong, R.R. Rao, K.A. Stoerzinger, Y. Shao-Horn, PH dependence of OER activity of oxides: Current and future perspectives, *Catal. Today*. 262 (2016) 2–10. <https://doi.org/10.1016/j.cattod.2015.10.006>.
- [23] J. Zheng, W. Sheng, Z. Zhuang, B. Xu, Y. Yan, Universal dependence of hydrogen oxidation and evolution reaction activity of platinum-group metals on pH and hydrogen binding energy, *Sci. Adv.* 2 (2016) 1–8.

- <https://doi.org/10.1126/sciadv.1501602>.
- [24] L. Li, S. Yin, L. Huang, X. Yi, Y. Wang, K. Zhang, C.G. Ooi, D.T. Allen, An emission inventory for Cl₂ and HOCl in Shanghai, 2017, *Atmos. Environ.* 223 (2020).
<https://doi.org/10.1016/j.atmosenv.2019.117220>.
- [25] L. Bigiani, D. Barreca, A. Gasparotto, T. Andreu, J. Verbeeck, C. Sada, E. Modin, O.I. Lebedev, J.R. Morante, C. Maccato, Selective anodes for seawater splitting via functionalization of manganese oxides by a plasma-assisted process, *Appl. Catal. B Environ.* 3373 (2020). <https://doi.org/10.1016/j.apcatb.2020.119684>.
- [26] C. Ros, T. Andreu, J.R. Morante, Photoelectrochemical water splitting: a road from stable metal oxides to protected thin film solar cells, *J. Mater. Chem. A.* (2020) 10625–10669. <https://doi.org/10.1039/d0ta02755c>.
- [27] M.S. Faber, S. Jin, Earth-abundant inorganic electrocatalysts and their nanostructures for energy conversion applications, *Energy Environ. Sci.* 7 (2014) 3519–3542.
<https://doi.org/10.1039/C4EE01760A>.
- [28] X. Gao, Y. Chen, T. Sun, J. Huang, W. Zhang, Q. Wang, R. Cao, Karst landform-featured monolithic electrode for water electrolysis in neutral media, *Energy Environ. Sci.* 13 (2020) 174–182. <https://doi.org/10.1039/c9ee02380a>.
- [29] J. Juodkazytė, B. Šebeka, I. Savickaja, M. Petrulevičienė, S. Butkutė, V. Jasulaitienė, A. Selskis, R. Ramanauskas, Electrolytic splitting of saline water: Durable nickel oxide anode for selective oxygen evolution, *Int. J. Hydrogen Energy.* 44 (2019) 5929–5939. <https://doi.org/10.1016/j.ijhydene.2019.01.120>.
- [30] Y. Kuang, M.J. Kenney, Y. Meng, W.H. Hung, Y. Liu, J.E. Huang, R. Prasanna, P. Li, Y. Li, L. Wang, M.C. Lin, M.D. McGehee, X. Sun, H. Dai, Solar-driven, highly

- sustained splitting of seawater into hydrogen and oxygen fuels, *Proc. Natl. Acad. Sci. U. S. A.* 116 (2019) 6624–6629. <https://doi.org/10.1073/pnas.1900556116>.
- [31] L. Yu, Q. Zhu, S. Song, B. McElhenny, D. Wang, C. Wu, Z. Qin, J. Bao, Y. Yu, S. Chen, Z. Ren, Non-noble metal-nitride based electrocatalysts for high-performance alkaline seawater electrolysis, *Nat. Commun.* 10 (2019) 1–10. <https://doi.org/10.1038/s41467-019-13092-7>.
- [32] F. Cheng, X. Feng, X. Chen, W. Lin, J. Rong, W. Yang, Synergistic action of Co-Fe layered double hydroxide electrocatalyst and multiple ions of sea salt for efficient seawater oxidation at near-neutral pH, *Electrochim. Acta.* 251 (2017) 336–343. <https://doi.org/10.1016/j.electacta.2017.08.098>.
- [33] A.A. El-Moneim, N. Kumagai, K. Asami, K. Hashimoto, Nanocrystalline manganese-molybdenum-tungsten oxide anodes for oxygen evolution in acidic seawater electrolysis, *Mater. Trans.* 46 (2005) 309–316. <https://doi.org/10.2320/matertrans.46.309>.
- [34] Z. Kato, J. Bhattarai, N. Kumagai, K. Izumiya, K. Hashimoto, Durability enhancement and degradation of oxygen evolution anodes in seawater electrolysis for hydrogen production, *Appl. Surf. Sci.* 257 (2011) 8230–8236. <https://doi.org/10.1016/j.apsusc.2010.12.042>.
- [35] C. Flox, S. Murcia-López, N.M. Carretero, C. Ros, J.R. Morante, T. Andreu, Role of Bismuth in the Electrokinetics of Silicon Photocathodes for Solar Rechargeable Vanadium Redox Flow Batteries, *ChemSusChem.* 11 (2018) 125–129. <https://doi.org/10.1002/cssc.201701879>.
- [36] S. Murcia-López, M. Chakraborty, N.M. Carretero, C. Flox, J.R. Morante, T. Andreu, Adaptation of Cu(In, Ga)Se₂ photovoltaics for full unbiased photocharge of integrated

- solar vanadium redox flow batteries, *Sustain. Energy Fuels*. 4 (2020) 1135–1142.
<https://doi.org/10.1039/c9se00949c>.
- [37] S. Gupta, M. Forster, A. Yadav, A.J. Cowan, N. Patel, M. Patel, Highly Efficient and Selective Metal Oxy-Boride Electrocatalysts for Oxygen Evolution from Alkali and Saline Solutions, (2020). <https://doi.org/10.1021/acsaem.0c01040>.
- [38] M.L.C.M. Henckens, P.P.J. Driessen, E. Worrell, Metal scarcity and sustainability, analyzing the necessity to reduce the extraction of scarce metals, *Resour. Conserv. Recycl.* 93 (2014) 1–8. <https://doi.org/10.1016/j.resconrec.2014.09.012>.
- [39] L. Trotochaud, S.L. Young, J.K. Ranney, S.W. Boettcher, Nickel-Iron oxyhydroxide oxygen-evolution electrocatalysts: The role of intentional and incidental iron incorporation, *J. Am. Chem. Soc.* 136 (2014) 6744–6753.
<https://doi.org/10.1021/ja502379c>.
- [40] D.Y. Chung, P.P. Lopes, P. Farinazzo Bergamo Dias Martins, H. He, T. Kawaguchi, P. Zapol, H. You, D. Tripkovic, D. Strmcnik, Y. Zhu, S. Seifert, S. Lee, V.R. Stamenkovic, N.M. Markovic, Dynamic stability of active sites in hydr(oxy)oxides for the oxygen evolution reaction, *Nat. Energy*. 5 (2020) 222–230.
<https://doi.org/10.1038/s41560-020-0576-y>.
- [41] T. Wang, R. Jin, X. Wu, J. Zheng, X. Li, K. Ostrikov, A highly efficient Ni-Mo bimetallic hydrogen evolution catalyst derived from a molybdate incorporated Ni-MOF, *J. Mater. Chem. A*. 6 (2018) 9228–9235. <https://doi.org/10.1039/c8ta01325j>.
- [42] C. Fan, Study of Electrodeposited Nickel-Molybdenum, Nickel-Tungsten, Cobalt-Molybdenum, and Cobalt-Tungsten as Hydrogen Electrodes in Alkaline Water Electrolysis, *J. Electrochem. Soc.* 141 (1994) 382. <https://doi.org/10.1149/1.2054736>.

- [43] I. Roger, M.A. Shipman, M.D. Symes, Earth-abundant catalysts for electrochemical and photoelectrochemical water splitting, *Nat. Rev. Chem.* 1 (2017).
<https://doi.org/10.1038/s41570-016-0003>.
- [44] Y.K. Li, G. Zhang, W.T. Lu, F.F. Cao, Amorphous Ni–Fe–Mo Suboxides Coupled with Ni Network as Porous Nanoplate Array on Nickel Foam: A Highly Efficient and Durable Bifunctional Electrode for Overall Water Splitting, *Adv. Sci.* 7 (2020).
<https://doi.org/10.1002/advs.201902034>.
- [45] C. Flox, J. Rubio-García, M. Skoumal, T. Andreu, J.R. Morante, Thermo-chemical treatments based on NH₃/O₂ for improved graphite-based fiber electrodes in vanadium redox flow batteries, *Carbon N. Y.* 60 (2013) 280–288.
<https://doi.org/10.1016/j.carbon.2013.04.038>.
- [46] Z. González, C. Flox, C. Blanco, M. Granda, J.R. Morante, R. Menéndez, R. Santamaría, Outstanding electrochemical performance of a graphene-modified graphite felt for vanadium redox flow battery application, *J. Power Sources.* 338 (2017) 155–162. <https://doi.org/10.1016/j.jpowsour.2016.10.069>.
- [47] J. Vázquez-Galván, C. Flox, J.R. Jervis, A.B. Jorge, P.R. Shearing, J.R. Morante, High-power nitrided TiO₂ carbon felt as the negative electrode for all-vanadium redox flow batteries, *Carbon N. Y.* 148 (2019) 91–104.
<https://doi.org/10.1016/j.carbon.2019.01.067>.
- [48] S. Tanpure, V. Ghanwat, B. Shinde, K. Tanpure, S. Lawande, The Eggshell Waste Transformed Green and Efficient Synthesis of K-Ca(OH)₂ Catalyst for Room Temperature Synthesis of Chalcones, *Polycycl. Aromat. Compd.* (2020).
<https://doi.org/10.1080/10406638.2020.1776740>.
- [49] A. Ansari, A. Ali, M. Asif, Shamsuzzaman, Microwave-assisted MgO NP catalyzed

- one-pot multicomponent synthesis of polysubstituted steroidal pyridines, *New J. Chem.* 42 (2018) 184–197. <https://doi.org/10.1039/c7nj03742b>.
- [50] Nikkei, (n.d.). <https://asia.nikkei.com>.
- [51] I. Roger, M.A. Shipman, M.D. Symes, Earth-abundant catalysts for electrochemical and photoelectrochemical water splitting Isolda, *Nat. Rev. Chem.* 1 (2017) 1–13. <https://doi.org/10.1038/s41570-016-0003>.
- [52] L. Bigiani, D. Barreca, A. Gasparotto, T. Andreu, J. Verbeeck, C. Sada, E. Modin, O.I. Lebedev, J. Ram, *Applied Catalysis B : Environmental* Selective anodes for seawater splitting via functionalization of manganese oxides by a plasma-assisted process, 284 (2021). <https://doi.org/10.1016/j.apcatb.2020.119684>.
- [53] D. Wintrich, D. Öhl, S. Barwe, A. Ganassin, S. Möller, T. Tarnev, A. Botz, A. Ruff, J. Clausmeyer, J. Masa, W. Schuhmann, Enhancing the Selectivity between Oxygen and Chlorine towards Chlorine during the Anodic Chlorine Evolution Reaction on a Dimensionally Stable Anode, *ChemElectroChem.* 6 (2019) 3108–3112. <https://doi.org/10.1002/celec.201900784>.
- [54] C. Ros, T. Andreu, J. David, J. Arbiol, J.R. Morante, Degradation and regeneration mechanisms of NiO protective layers deposited by ALD on photoanodes, *J. Mater. Chem. A.* 7 (2019) 21892–21902. <https://doi.org/10.1039/c9ta08638b>.
- [55] K. Zhu, W. Luo, G. Zhu, J. Wang, Y. Zhu, Z. Zou, W. Huang, Interface-Engineered Ni(OH)₂/β-like FeOOH Electrocatalysts for Highly Efficient and Stable Oxygen Evolution Reaction, *Chem. - An Asian J.* 12 (2017) 2720–2726. <https://doi.org/10.1002/asia.201700964>.
- [56] O. Diaz-Morales, Impurity as a virtue, *Nat. Energy.* 5 (2020) 193–194.

- <https://doi.org/10.1038/s41560-020-0585-x>.
- [57] M. Bonomo, G. Naponiello, D. Dini, Oxidative dissolution of NiO in aqueous electrolyte: An impedance study, *J. Electroanal. Chem.* 816 (2018) 205–214. <https://doi.org/10.1016/j.jelechem.2018.03.058>.
- [58] S. Leroy, F. Blanchard, R. Dedryvère, H. Martinez, B. Carré, D. Lemordant, D. Gonbeau, Surface film formation on a graphite electrode in Li-ion batteries: AFM and XPS study, *Surf. Interface Anal.* 37 (2005) 773–781. <https://doi.org/10.1002/sia.2072>.
- [59] D.W. Lee, L. De Los Santos V., J.W. Seo, L.L. Felix, A. Bustamante D., J.M. Cole, C.H.W. Barnes, The structure of graphite oxide: Investigation of its surface chemical groups, *J. Phys. Chem. B.* 114 (2010) 5723–5728. <https://doi.org/10.1021/jp1002275>.
- [60] S. Balamurugan, N. Naresh, I. Prakash, N. Satyanarayana, Capacity fading mechanism of Li₂O loaded NiFe₂O₄/SiO₂ aerogel anode for lithium-ion battery: Ex-situ XPS analysis, *Appl. Surf. Sci.* 535 (2021). <https://doi.org/10.1016/j.apsusc.2020.147677>.
- [61] M.C. Biesinger, B.P. Payne, L.W.M. Lau, A. Gerson, R.S.C. Smart, X-ray photoelectron spectroscopic chemical state Quantification of mixed nickel metal, oxide and hydroxide systems, *Surf. Interface Anal.* 41 (2009) 324–332. <https://doi.org/10.1002/sia.3026>.
- [62] M. Theses, C.H. Chi, The anodic dissolution of molybdenum in alkaline solutions, *Electroanalytical Chem. Interfacial Electrochem.* 1 (1969) 121–130.
- [63] Y. Wu, H. He, Electrodeposited nickel–iron–carbon–molybdenum film as efficient bifunctional electrocatalyst for overall water splitting in alkaline solution, *Int. J. Hydrogen Energy.* 44 (2019) 1336–1344. <https://doi.org/10.1016/j.ijhydene.2018.11.168>.

- [64] C. Xie, Y. Wang, K. Hu, L. Tao, X. Huang, J. Huo, S. Wang, In situ confined synthesis of molybdenum oxide decorated nickel-iron alloy nanosheets from MoO₄²⁻ intercalated layered double hydroxides for the oxygen evolution reaction, *J. Mater. Chem. A*. 5 (2017) 87–91. <https://doi.org/10.1039/c6ta08149e>.
- [65] I.A. Raj, K.I. Vasu, Transition metal-based hydrogen electrodes in alkaline solution - electrocatalysis on nickel based binary alloy coatings, *J. Appl. Electrochem.* 20 (1990) 32–38. <https://doi.org/10.1007/BF01012468>.
- [66] J.A. Bau, S.M. Kozlov, L.M. Azofra, S. Ould-Chikh, A.H. Emwas, H. Idriss, L. Cavallo, K. Takanabe, Role of Oxidized Mo Species on the Active Surface of Ni-Mo Electrocatalysts for Hydrogen Evolution under Alkaline Conditions, *ACS Catal.* (2020) 12858–12866. <https://doi.org/10.1021/acscatal.0c02743>.
- [67] J.D. Rodriguez-Blanco, S. Shaw, P. Bots, T. Roncal-Herrero, L.G. Benning, The role of pH and Mg on the stability and crystallization of amorphous calcium carbonate, *J. Alloys Compd.* 536 (2012) S477–S479. <https://doi.org/10.1016/j.jallcom.2011.11.057>.
- [68] G. Hanrahan, L. Angeles, *CRC Handbook of Chemistry and Physics*, 86th Edition Edited by David R. Lide (National Institute of Standards and Technology). CRC Press (an imprint of Taylor and Francis Group): Boca Raton, FL. 2005. 2544 pp. \$125.96. ISBN 0-8493-0486-5., *J. Am. Chem. Soc.* 128 (2006) 5585–5585. <https://doi.org/10.1021/ja059868l>.
- [69] Sulfuric Acid Price Analysis CAS No.: 7664-93-9, (n.d.). https://www.echemi.com/productsInformation/pid_Rock19440-sulfuric-acid.html.

Accepted Manuscript